FORMATION FLIGHT OF FIXED-WING UAVS USING ARTIFICIAL POTENTIAL FIELD

Yoshitsugu Nagao*and Kenji Uchiyama*
*Department of Aerospace Engineering, Nihon University csyo12017@g.nihon-u.ac.jp, uchiyama@aero.cst.nihon-u.ac.jp

Keywords: UAV, Formation Flight, Potential Function Method, Velocity Field

Abstract

This paper describes the design of guidance law using potential functions for a swarm of Unmanned Aerial Vehicles (UAVs). proposed guidance law is derived by the artificial potential field method. We propose a new potential function that consists of steering, repulsive, and circular functions. A guidance law is obtained by generating a velocity fields from the gradient of the proposed potential function. The developed fixed-wing UAV is equipped with an inertial measurement unit, a GPS. microcomputer. and radio communication module. The validity of the proposed guidance law is verified by numerical simulations. The experiment of formation flight is also demonstrated using the developed UAV.

1 Introduction

UAVs have been used for a pesticide application. scientific atmospheric collection or observation from the air. A flight system using multiple UAVs is attracting much attention due to the advantages of extending coverage, improving connectivity for long-range communications, and fault tolerance for a cooperative work. The system should design a flight path to generate an optimal formation pattern for a mission and for avoidance of obstacles and in-flight collision. In order to achieve the formation flight, each UAV needs information relating to position to avoid each other. This eventually leads to constructing a complicated system due to much data supplied for the computation. Moreover, it would be difficult for the system to correspond to an unexpected accident when generating a flight path. Therefore, a simple design method is preferable for the complicated flight control system.

Artificial potential fields [1-4] have been applied to derivation of a guidance law for a formation flight. The guidance law using, which is simple and fast to compute, can allow different patterns to be formed through change of a parameter in a potential function. The flight system in the case of circular pattern formation, however, has ability to be unstable because desired heading angle varies violently around equilibrium state. To overcome this problem we define a new potential function that is regarded as circular potential [5-7] using a sigmoid function. The numerical simulation of a formation flight is performed to verify the validity of the proposed guidance law. Moreover, we develop the UAVs having an autonomous flight control. Experiments using the fixed-wing UAV are also demonstrated by applying the potential function to a velocity field.

2 Guidance and Control System

2.1 Guidance Law

We use potential functions to find a guidance law for formation flight of UAVs. The potential functions can generate artificial potential fields. In this paper, we apply the potential function to a velocity field to obtain command values. Desired velocities for a formation flight are calculated by partial derivative of the potential functions with respect to position. The velocity field for UAVs \mathbf{v}_i is generated by the steering potential function U^S , the repulsive potential

function U^R and the circular potential function U^C .

The velocity field that is obtained from the potential function is described by the following equation.

$$\mathbf{v}_{i} = -\nabla_{i} U^{S}(\mathbf{x}_{i}) - \nabla_{i} U_{ij}^{R}(\mathbf{x}_{ij}) + \widetilde{\nabla}_{i} \mathbf{U}^{C}$$
 (1)

where \mathbf{x}_i represents the position vector and $\mathbf{x}_{ij} = |\mathbf{x}_i - \mathbf{x}_j|$ denotes relative distance between i-th UAV and j-th UAV or obstacle. $\widetilde{\nabla}$ represents skew-symmetric matrix and $\mathbf{U}^C = [0 \ 0 \ U^C]^T$ denotes a vector of a circular potential function.

The steering potential function U^S guides the UAV on a desired position ρ_d . The function U^S is defined as Eqs. (2) and (3).

$$U^{S}(x_{i}, y_{i}) = C_{h} \left(\sqrt{(\rho_{i} - \rho_{d})^{2} + 1} + \sqrt{\sigma_{i} + 1} \right)$$

$$(2)$$

$$U^{S}(z_{i}) = C_{hz} \left(\sqrt{(\rho_{i} - \rho_{d})^{2} + 1} + \sqrt{\sigma_{i} + 1} \right)$$

$$(3)$$

Design parameters of the function C_h and C_{hz} in Eqs. (2) and (3) are variables which coincide with the maximum induced velocity on the vector field. Formation patterns can be determined by the parameter ρ_i expressed by following equations.

$$\rho_i = x_i \text{ or } y_i \text{ or } z_i \quad \text{(for line formation)}$$

$$\rho_i = \sqrt{x_i^2 + y_i^2 + z_i^2} \text{ (for ring formation)}$$
 (5)

 σ_i changes the formation plane to threedimensionally, and it is defined by the following equation.

$$\sigma_i = ax_i + by_i + cz_i \tag{6}$$

where a, b and c represent the vector components of σ_i . Three-dimensional formation flying can be achieved by manipulating parameters a, b and c which can change the angle of the formation pattern. If a=1 and b=c=0, b=1 and a=c=0, and c=1 and a=b=0, the formation patterns are generated in the y-z, z-x, and x-y planes, respectively.

Figures 1 (a) to (d) show examples of steering potential fields for line and ring formation and those velocity fields. It is noted that the steering potential function U^S has one state of dynamical equilibrium at a desired position ρ_d . It can be seen that direction of velocity vectors are faced to the desired position ρ_d vertically as shown in Figs.1 (b) and (d).

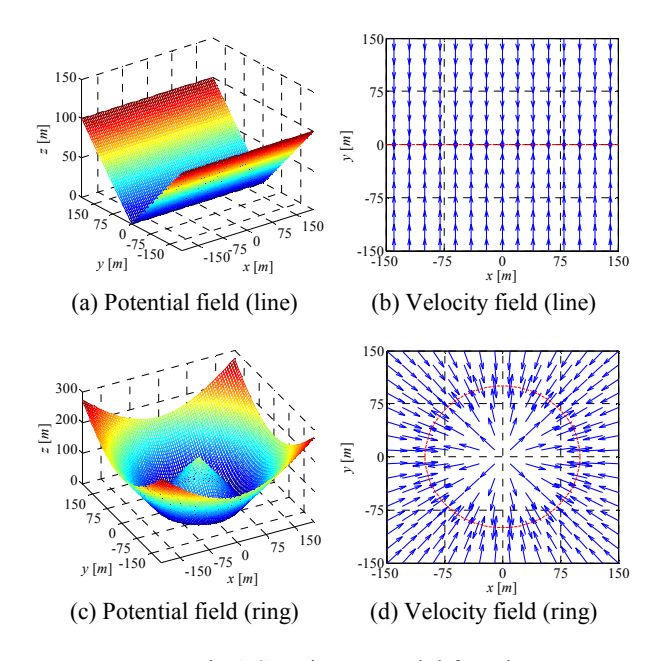


Fig.1 Steering potential function

The repulsive potential function U^R is defined as Eq. (7) and (8) using an exponential function.

$$U_{ij}^{R}(x_i, y_i) = C_r \sum_{j, i \neq i} \exp\left(-\frac{|\mathbf{x}_{ij}|}{L_r}\right)$$
 (7)

$$U_{ij}^{R}(z_i) = C_{rz} \sum_{i,i \neq i} \exp\left(-\frac{\left|\mathbf{x}_{ij}\right|}{L_r}\right)$$
(8)

where C_r and C_{rz} denote the amplitude and L_r denotes length scale of the repulsive potential function.

The total repulsive bound velocity on a UAV is dependent on the position of the other UAVs during formation flight. The repulsive potential function U^R is, therefore, used to ensure that UAVs are steered towards the goal state as they do not collide with each other.

Figure 2 (a) and (b) show an example of repulsive potential field and the velocity field. Figure 2 (a) shows repulsive point that has the highest potential. In Fig.2 (b), it can be seen that direction of velocity vectors are faced to opposite side of the repulsive point.

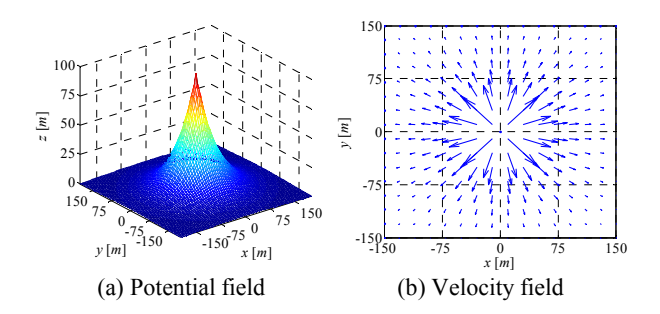


Fig.2 Repulsive Potential Function

UAVs can perform the line flight in those potential functions. However, the potential function generates sometimes unstable command when the UAV across equilibrium state in a circular flight. Thus, it is necessary to generate a command which prompt the circular flight. The potential function is redesigned to obtain stable commands by applying the circular potential function U_c . The circular potential function U_c is defined as follow using a sigmoid function.

$$U^{C} = \frac{C_{c}}{1 + \exp(L_{C}(\rho_{i} - \rho_{d}))}$$
(9)

where C_c denotes the amplitude and the direction of rotation and L_c is length scale of the circulate.

Figure 3 (a) and (b) show an example of circular potential field and the velocity field. Figure 3 (b) shows a velocity field for a circular flight is generated around the guidance circle from circular potential field.

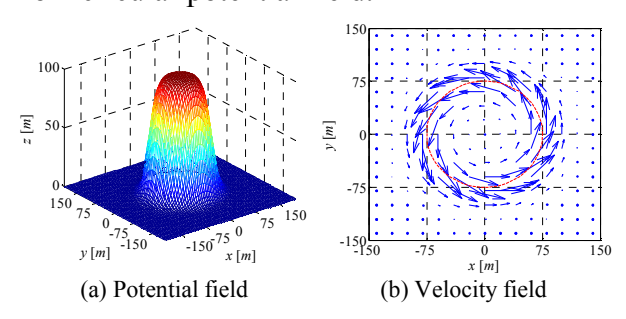


Fig.3 Circular potential function

Figure 4 shows a reference design of a velocity field that uses those potential functions. In this numerical simulation, an obstacle is imaginarily set at (x, y) = (-75,0) and a radius of guidance circle is defined as 75[m]. It can be seen that stable commands are obtained by using those potential functions.

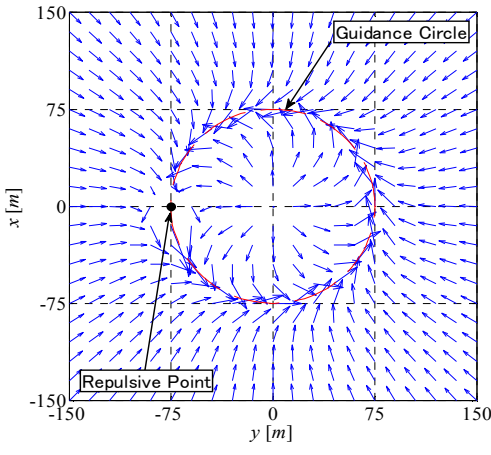


Fig.4 Velocity Field

The command value of heading angle $\psi_{d,i}$, speed of x axis $u_{d,i}$ and z axis $w_{d,i}$ of each UAV are expressed as follows:

$$\psi_{d,i} = \tan^{-1} \left(\frac{v_{y,i}}{v_{x,i}} \right) \tag{10}$$

$$u_{d,i} = \sqrt{u_{x,i}^2 + u_{y,i}^2} \tag{11}$$

$$w_{d,i} = u_{z,i}^2 \tag{12}$$

Velocity vectors for a formation flight are described as Eqs. (13) to (17)

$$v_{x,i} = -\frac{\partial U^{S}(x_{i})}{\partial x_{i}} - \frac{\partial U_{ij}^{R}(x_{ij})}{\partial x_{i}} - \frac{\partial U^{C}}{\partial y_{i}}$$
(13)

$$v_{y,i} = -\frac{\partial U^{S}(y_{i})}{\partial y_{i}} - \frac{\partial U_{ij}^{R}(y_{ij})}{\partial y_{i}} - \frac{\partial U^{C}}{\partial x_{i}}$$
(14)

$$u_{x,i} = -\frac{\partial U^{S}(x_{i})}{\partial x_{i}} - \frac{\partial U_{ij}^{R}(x_{ij})}{\partial x_{i}}$$
(15)

$$u_{y,i} = -\frac{\partial U^{S}(y_{i})}{\partial y_{i}} - \frac{\partial U_{ij}^{R}(y_{ij})}{\partial y_{i}}$$
(16)

$$u_{z,i} = -\frac{\partial U^{S}(z_{i})}{\partial z_{i}} - \frac{\partial U_{ij}^{R}(z_{ij})}{\partial z_{i}}$$
(17)

However, the UAV should take a bank angle into consideration when it flies circular flight. According to equilibrium of steady level turning flight, a bank angle of circular flight is expressed as Eq. (18)

$$\phi_0 = \tan^{-1} \left(\frac{u^2}{g\rho_i} \right) \tag{18}$$

Using the bank angle in Eq.(18), the command value of bank angle $\phi_{d,i}$ is expressed by Eq. (19). Here L_b is length scale of the command bank angle.

$$\phi_{d,i} = \phi_0 \exp\left(-\exp\left(-\frac{(\rho_i - \rho_d)}{L_b}\right) - \frac{(\rho_i - \rho_d)}{L_b} + 1\right)$$
(19)

2.2 UAV Dynamics

Figure 5 shows the definitions of the state variables and control inputs. u, v and w are velocities along roll axis, pitch axis, and yaw axis, respectively. ϕ , θ and ψ denote roll, pitch and yaw angles. p, q and r are those rates. The UAV has control surfaces, which are ailerons, rudder and elevator, and propulsion system that employs a propeller attached near the centre of mass. δ_a , δ_r , δ_e , and δ_t are deflections of moving surfaces from a trim, and thrust, respectively.

In order to simulate numerically a formation flight of UAVs, we use a model for the UAV that is linearized around steady flight condition. Equations (20) and (21) show longitudinal motion and lateral motion of UAV, respectively.

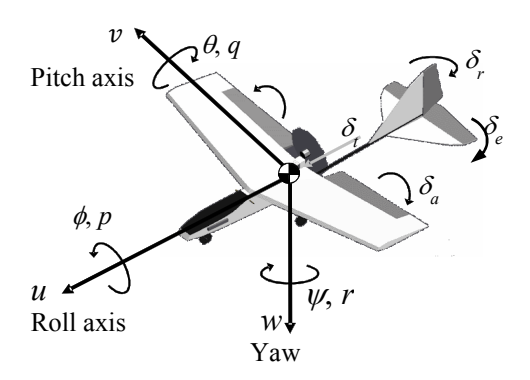


Fig.5 Body Fixed Coordinate System of UAV

$$\begin{bmatrix} u \\ w \\ q \\ \theta \end{bmatrix} = \begin{bmatrix} X_u & X_w & -W_0 & -g\cos\theta_0 \\ Z_u & Z_w & U_0 + Z_q & -g\sin\theta_0 \\ M_u & M_w & M_q & 0 \\ 0 & 0 & 1 & 0 \end{bmatrix} \begin{bmatrix} u \\ w \\ q \\ \theta \end{bmatrix} \\ + \begin{bmatrix} X_{\delta_e} & X_{\delta_t} \\ Z_{\delta_e} & Z_{\delta_t} \\ M_{\delta_e} & M_{\delta_t} \\ 0 & 0 \end{bmatrix} \begin{bmatrix} \delta_e \\ \delta_t \end{bmatrix}$$
 (20)

$$\begin{bmatrix} v \\ p \\ r \\ \phi \\ \psi \end{bmatrix} = \begin{bmatrix} Y_{v} & Y_{p} & Y_{r} - U_{0} & g \cos \theta_{0} & 0 \\ L_{v} & L_{p} & L_{r} & 0 & 0 \\ N_{v} & N_{p} & N_{r} & 0 & 0 \\ 0 & 1 & \tan \theta_{0} & 0 & 0 \\ 0 & 0 & \sec \theta_{0} & 0 & 0 \end{bmatrix} \begin{bmatrix} v \\ p \\ r \\ \phi \\ \psi \end{bmatrix}$$

$$+ \begin{bmatrix} Y_{\delta_{a}} & Y_{\delta_{r}} \\ L_{\delta_{a}} & L_{r} \\ N_{\delta_{a}} & N_{\delta r} \\ 0 & 0 \\ 0 & 0 \end{bmatrix} \begin{bmatrix} \delta_{a} \\ \delta_{r} \end{bmatrix}$$
 (21)

It is necessary to identify stability derivatives of the UAV. The stability derivatives normally can be determined by a wind tunnel experiment. However, it is difficult to obtain accurate data in terms of the derivatives of a small size UAV that flies in low Reynolds number because measurement signals of force are also significantly small and include noise and uncertainties.

On the other hand, the estimation formulas of stability derivatives are derived under the assumption of flight in subsonic range. It may be noted that this method is also not appropriate for small size UAVs. However, the formula is useful because the stability derivatives can be obtained by geometrical information and physical quantities such as weight and inertial moment of a UAV. Tables 1 and 2 show the results of calculation of the derivatives of the developed UAV model.

3 Numerical Simulations

We developed a UAV as described later to verify the validity of the proposed control method experimentally. We conduct numerical simulations under same experimental condition as much as possible. The forward speed of steady flight is set as 12.5 [m/s]. A saturation values of control inputs, δ_a , δ_r , δ_e , and δ_t are set as $\pm 30 [\text{deg}]$, $\pm 50 [\text{deg}]$, $\pm 35 [\text{deg}]$ and $\pm 1 [\text{N}]$.

Table.1 Stability Derivatives for Longitudinal Motion

Derivative		Estimation
X_u	[s ⁻¹]	-0.29
X_w	[s ⁻¹]	0.89
W_0	[ms ⁻¹]	0
Z_u	[s ⁻¹]	-3.70
Z_w	[s ⁻¹]	16.95
U_0	[ms ⁻¹]	12.5
Z_q	[ms ⁻¹]	-11.596
M_u	[ms ⁻¹]	2.61
M_w	[ms ⁻¹]	-55.17
M_q	[s ⁻¹]	-43.34
$X_{\delta e}$	[ms ⁻²]	0
$X_{\delta t}$	$[kg^{-1}]$	2.12
$Z_{\delta e}$	[ms ⁻²]	-18.72
$Z_{\delta t}$	$[kg^{-1}]$	0
$M_{\delta e}$	[s ⁻²]	-532.76
$M_{\delta t}$	[kg ⁻¹ m ⁻¹]	-7.16

State quantities of the developed UAV such as velocities should be estimated by using an observer. We perform numerical simulations in two cases to verify the validity of the proposed method.

Case 1 treats ring formation flight of three UAVs using the steering potential and the repulsive potential. It is noted that the proposed potential field moves at a forward speed of 12.5[m/s] as same as the speed of steady flight of the UAV.

Case 2 employs a potential functions that consists of the steering potential, the repulsive potential, and the circular potential. The designed potential field keeps its position on the inertial coordinate system unlike the case 1. The proposed command bank angle in Eq.(18) is derived in this case.

3.1 Results of Case1

Figures 6 to 9 show the results of numerical simulation of Case 1. We change the formation patterns every 50 seconds. The desired radius of ring formation is varied according to the order of r = 10[m], r = 0[m], and r = 15[m]. The design parameters of steering potential and repulsive potential are set as $C_h = 1$, $C_{hz} = 5$, $C_r = 10$, $C_{rz} = 10$, and $L_r = 4$. The dimension of the formation pattern is set as c = 1 and a = b = 0 that is x-v plane.

Figure 6 shows the flight trajectories of three UAVs. The triangles in the figure denote every 10 seconds. The relative distance of each

Table.2 Stability Derivatives for Lateral Motion

Derivative		Estimation
Y_{ν}	[s ⁻¹]	-0.77
Y_p	[s ⁻¹]	0.064
Y_r	$[s^{-1}]$	0.35
L_{v} '	$[s^{-1}]$	-7.17
L_p '	[ms ⁻¹]	-34.21
L_r '	[ms ⁻¹]	6.25
N_{ν} '	[ms ⁻¹]	8.11
N_p '	[ms ⁻¹]	-0.82
N_r '	[s ⁻¹]	-4.23
$Y_{\delta r}$	[ms ⁻²]	3.95
$L_{\delta a}$ '	[kg ⁻¹]	504.52
$L_{\delta r}$ '	[ms ⁻²]	-4.93
$N_{\delta a}$ '	[kg ⁻¹]	5.46
$N_{\delta a}$ '	[s ⁻²]	-45.64

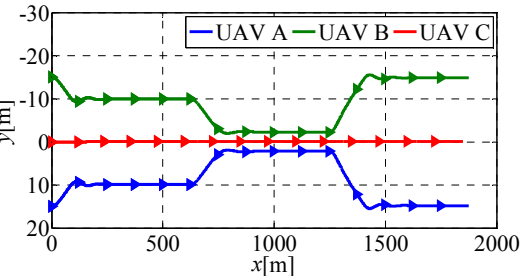


Fig.6 Flight Trajectories of UAVs (Case 1)

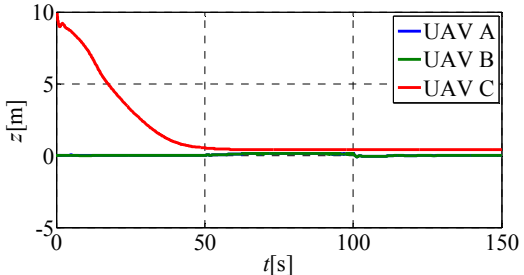


Fig.7 Time History of Altitudes (Case 1)

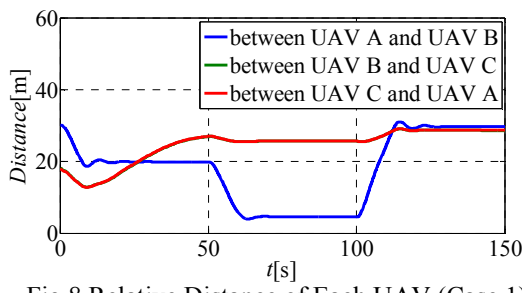


Fig.8 Relative Distance of Each UAV (Case 1)

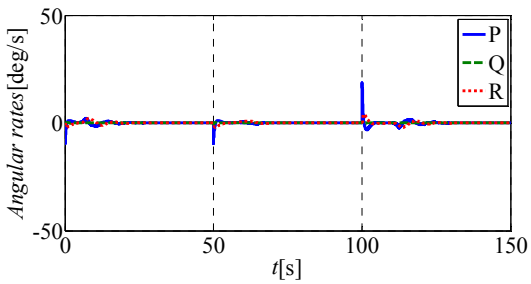


Fig.9 Time Histories of Angular Rates (UAV A)

UAV varies with time due to the change of radius of ring formation.

Figure 7 shows the time histories of altitude of UAVs. In this study, the origin of z axis, i.e. x-y plane, is defined at 70 [m] above sea level. Figure 8 shows the time history of distance between UAVs. It can be seen from Figs. 7 and 8 that each UAV is controlled to x-y plane and follows the desired position.

Figure 9 shows the angular rates of UAV A. It is clear from the figure that each UAV never collide because of repulsive potential function. Angular rates of the other UAVs are obtained as similar result with respect to UAV A.

3.2 Results of Case2

Figures 10 to 13 show the numerical result of Case 2. A radius of the guidance circle is 75[m]. The simulation parameters for each UAV are set as $C_h = 0.5$, $C_{hz} = 7.5$, $C_r = 10$, $C_{rz} = 150$, $L_r = 10$, $C_c = -100$ and $L_b = 10$. The dimension of the formation pattern is set as c = 1 and a = b = 0 that is x-y plane.

Figure 10 shows the flight trajectories of UAVs. Each UAV flies counter clockwise around the guidance circle that is designed using a steering potential, a repulsive potential and a circular potential. The triangles in the figure denote position of each UAV every 10 seconds. Start position of UAV A is inside of the guidance circle. Contrarily, UAV B and UAV C are outside of the circle at the beginning of the numerical simulation.

Figure 11 shows the time histories of altitude of UAVs. The altitude of all UAVs converges to the desired value 0 [m] that means 70 [m] above sea level.

Figure 12 shows the time histories of relative distance between UAVs. Each UAV does not fly at equal intervals because the distance is not controlled actively. The relative distance can be controlled by regulating design parameters of the repulsive potential function. It is clear from the figure that each UAV never collide due to the effectiveness of the repulsive potential function.

Figure 13 shows time histories of the angular rates of UAV A. The UAVs are guided to the guidance circle correctly. It can be seen

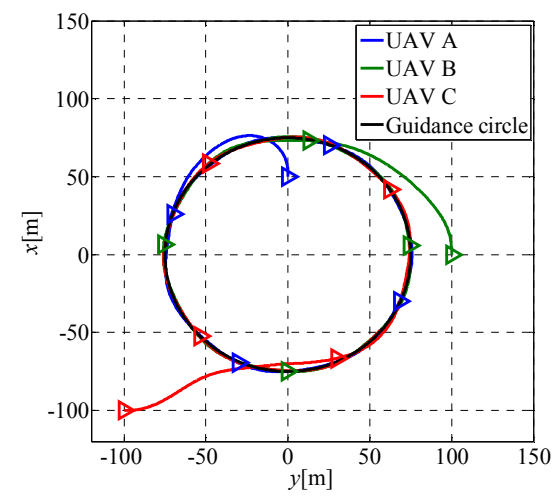


Fig. 10 Flight Trajectories of UAVs (Case 2)

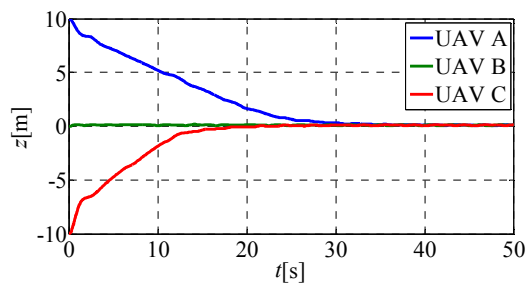


Fig. 11 Time Histories of Altitude (Case 2)

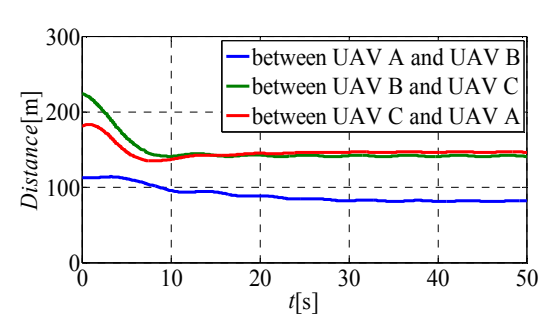


Fig. 12 Relative Distance of each UAV (Case 2)

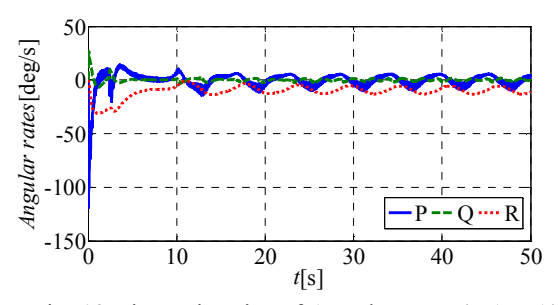


Fig. 13 Time Histories of Angular rates (UAV A)

from the figure that the angular rates of the UAV converge around 0 [deg/s].

The effectiveness of the potential function can be verified from these numerical results both cases.

4 Experiment

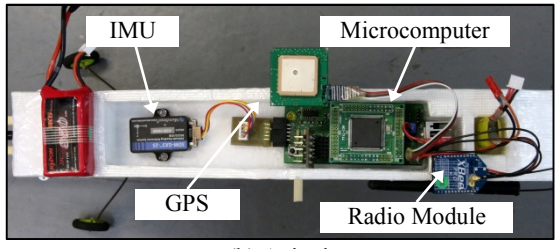
4.1 Developed UAV

In order to verify the guidance law using the potential function method, we have developed a UAV. Figure 14 (a) shows overview of the UAV with wing span 940 [mm]. The material of the wing, moving surfaces, and the fuselage of the UAV is EPP. The total mass including avionics is less than 600 [g].



Specification of UAV Wingspan: 940 [mm] Length: 900 [mm] Mass: 598 [g]

(a) Overview



(b) Avionics
Fig.14 Developed UAV

The avionics that is used in the developed UAV is shown in Fig.14 (b). The avionics consists of an inertial measurement unit (IMU), a GPS module, a 32-bit microcomputer, and a radio module.

The IMU measures the Euler angles ϕ , θ and ψ , and those rates p, q, and r around three axes of body-fixed coordinate system. The GPS module provides the position data such as the longitude, latitude and altitude of UAV. The microcomputer controls the UAV with sampling time 0.05 [s] according to a program with which we load the microcomputer. Each UAV can communicate by using the radio module through a developed grand station as shown in Fig.15.

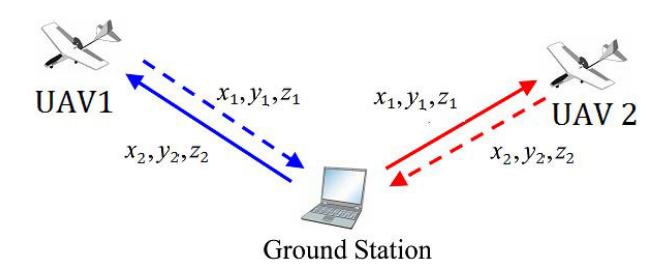


Fig.15 Intercommunication System

4.2 Experimental Result

For verification of the validity of the proposed guidance law, we demonstrate experiment of autonomous formation flight using two UAVs by applying a potential function to a velocity field. The circular potential function is used to avoid that the flight control system becomes unstable as mentioned before. The command values, which is derived using the velocity field, for guidance of the UAVs such as heading angle defined by Eq.(10) depends on its position measured by a GPS module.

The parameters for each UAV are set as same parameters in numerical simulation Case 2. It is supposed that both UAVs have the same parameters. A radius of the guidance circle is designed as 75[m]. The take-off of the UAV is performed manually, and then the UAV is switched to autonomous flight control.

Figure 16 shows the experimental results of UAVs' trajectories of autonomous formation flight. There is deviation between the guidance circle and trajectories of UAVs because of wind disturbance. It should be noted that the UAVs are controlled to the guidance circle despite the disturbance.

Figure 17 shows time histories of altitude of each UAV. It can be seen that the altitude of both UAVs are controlled around the target value 0 [m] although the small vibration with respect to the time histories is recognized.

Figure 18 shows relative distance between UAV A and UAV B. Figures 19 and 20 show time histories of angular rates of the UAVs. Although experimental data with high frequency noise is larger than the numerical results, the attitude of the UAVs is controlled stably with keeping the relative distance.

These experimental results show that effectiveness of the proposed guidance law is confirmed.

5 Conclusions

We apply the proposed guidance law based on the artificial potential field to the formation flight of the multiple fixed-wing UAVs. The results of the numerical simulation show the validity of the proposed flight control system. Experiment was demonstrated by using

developed UAVs. The experimental results show that the flight control system for the UAV works well. In future work, experiments will be performed using increased number of UAVs and a formation flight of UAVs will be demonstrated to change the formation pattern during those flights.

References

- [1] Bennet D. and McInnes C. R., "Space Craft Formation Flying Using Bifurcating Potential Fields," *International Astronautical Congress*, IAC-08-C1.6.4, 2008.
- [2] Bennet D. and McInnes C. R., "Pattern Transition in Spacecraft Formation Flying via The Artificial Potential Field Method and Bifurcation Theory," 3rd International Symposium on Formation Flying, Missions and Technologies, 2008.
- [3] Suzuki M., Uchiyama K., Bennet J., and McInnes C. R., "Three-Dimensional Formation Flying Using Bifurcating Potential fields," AIAA Guidance, Navigation, and Control Conference, AIAA-2009-5884, 2009.
- [4] M. Kokume and K. Uchiyama, "Guidance Law Based on Bifurcating Velocity Field for Formation Flight," *AIAA Guidance, Navigation, and Control Conference*, AIAA 2010-8081, 2010.
- [5] Nelson D. R., Barber D. B., McLain T. W., and Beard R. W., "Vector Field Path Following for Miniature Air Vehicles," *IEEE Transactions on Robotics*, Vol.23, No.3, 2007.
- [6] Frew E. W., Lawrence D. A., Dixon C., Elston J., and Pisano W. J., "Lyapunov Guidance Vector Fields for Unmanned Aircraft Applications," *IEEE American Control Conference*, 2007.
- [7] Barnes, Laura E., "A potential field based formation control methodology for robot swarms," *Dissertation at University of south Florida*, Paper 131, 2008.

Copyright Statement

The authors confirm that they, and/or their company or organization, hold copyright on all of the original material included in this paper. The authors also confirm that they have obtained permission, from the copyright holder of any third party material included in this paper, to publish it as part of their paper. The authors confirm that they give permission, or have obtained permission from the copyright holder of this paper, for the publication and distribution of this paper as part of the ICAS 2014 proceedings or as individual off-prints from the proceedings

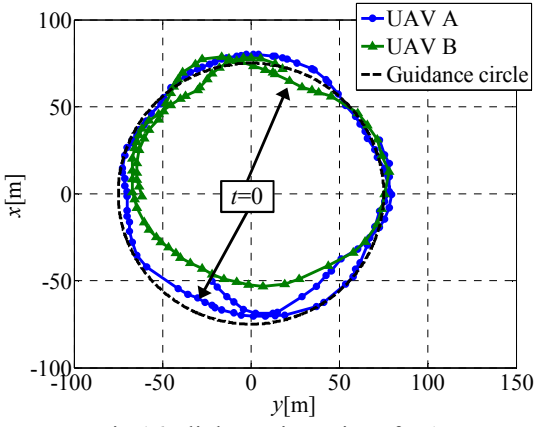


Fig.16 Flight Trajectories of UAVs

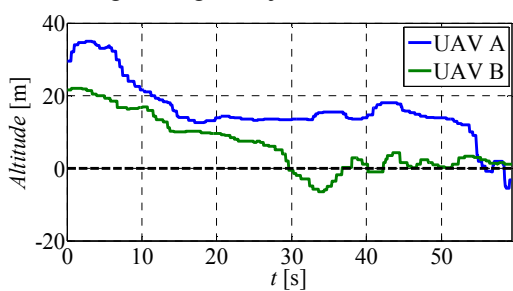


Fig. 17 Time Histories of Altitude

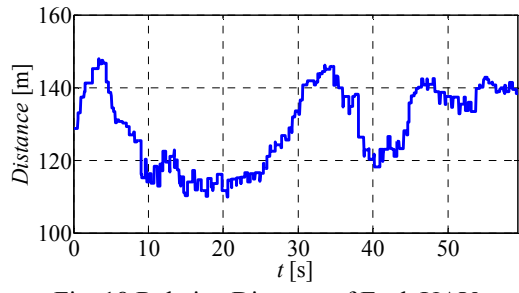


Fig. 18 Relative Distance of Each UAV

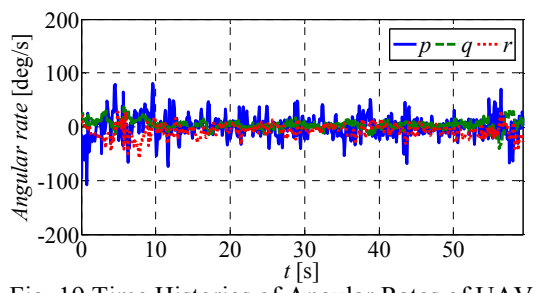


Fig. 19 Time Histories of Angular Rates of UAV A

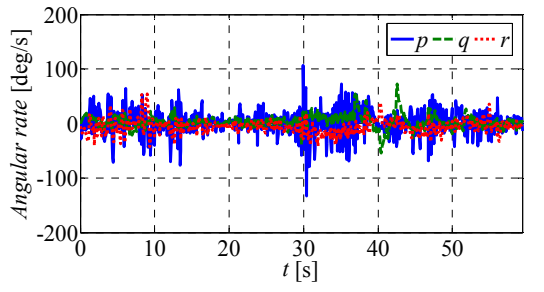


Fig. 20 Time History of Angular Rates of UAV B